Generation and reversal of surface flows by propagating waves

Horst Punzmann, Nicolas Francois, Hua Xia, Gregory Falkovich[1], and Michael Shats

Research School of Physics and Engineering, The Australian National University, Canberra, ACT 0200, Australia

[1] *Weizmann Institute of Science, Rehovot 76100 Israel and Institute for Information Transmission Problems, Moscow 127994 Russia*

This file contains Supplementary text (Sections 1-4) and Supplementary Figures 1-8.

S1   Wave generation and modulation instability of surface waves

Waves are generated by vertically oscillating plungers of different shapes. Spatially localized time-periodic perturbations of water surface generate waves propagating away from the plungers. The frequency of the plunger oscillations is varied in the range between 10 Hz, corresponding to gravity waves, and 200 Hz, corresponding to capillary waves. The dispersion relation is given by $\omega = (gk)^{1/2}$ for gravity waves, and $\omega = (\alpha k^3 / \rho)^{1/2}$ for capillary waves. Here g is the acceleration of gravity, α is the surface tension and ρ is the fluid density.

Both these branches of the surface waves are unstable with respect to the modulation instability, known as Benjamin-Feir instability for gravity waves [1], which develops when the Lighthill criterion is satisfied:

$$(\partial\omega / \partial|a|^2)(\partial^2\omega_k / \partial k^2) < 0 \qquad (1)$$

The nonlinear frequency corrections $(\partial\omega / \partial|a|^2)$ have different signs for different branches: positive for gravity waves, and negative for capillary waves [2]. Since the dispersion of the group velocity $(\partial^2\omega_k / \partial k^2)$ is negative for gravity waves and positive for capillary waves, the Lighthill criterion (1) is satisfied for both branches.

The transition from linear 2D regime to 3D wave fields, which is described in the main text (Figs. 1a,b), has been studied before in Ref. [3] where it has been shown that the increase in the plunger acceleration $a_c = A\omega_0^2 / g$ (where A is a peak-to-peak displacement of a plunger and $f_0 = \omega_0 /(2\pi)$ is the driving frequency) leads to the development of the instability and appearance of the cross-wave in the nonlinear stage [4]. The cross-wave instability modulates wave fronts in the transverse direction, destroying two-dimensionality of the wave and breaking it into individual pulses, which then propagate away from the source. These propagating wave pulses oscillate vertically with half the driving frequency, $f = f_0 / 2$, as expected for parametrically excited waves. The development of the cross-wave and the evolution of the wave spectra [3] are shown in Fig. S1. The surface wave spectra are obtained by using the laser reflection technique, which measures the gradient of the surface elevation. The wave fields are also visualized using the diffusive light imaging technique, Figs. S1g,h.
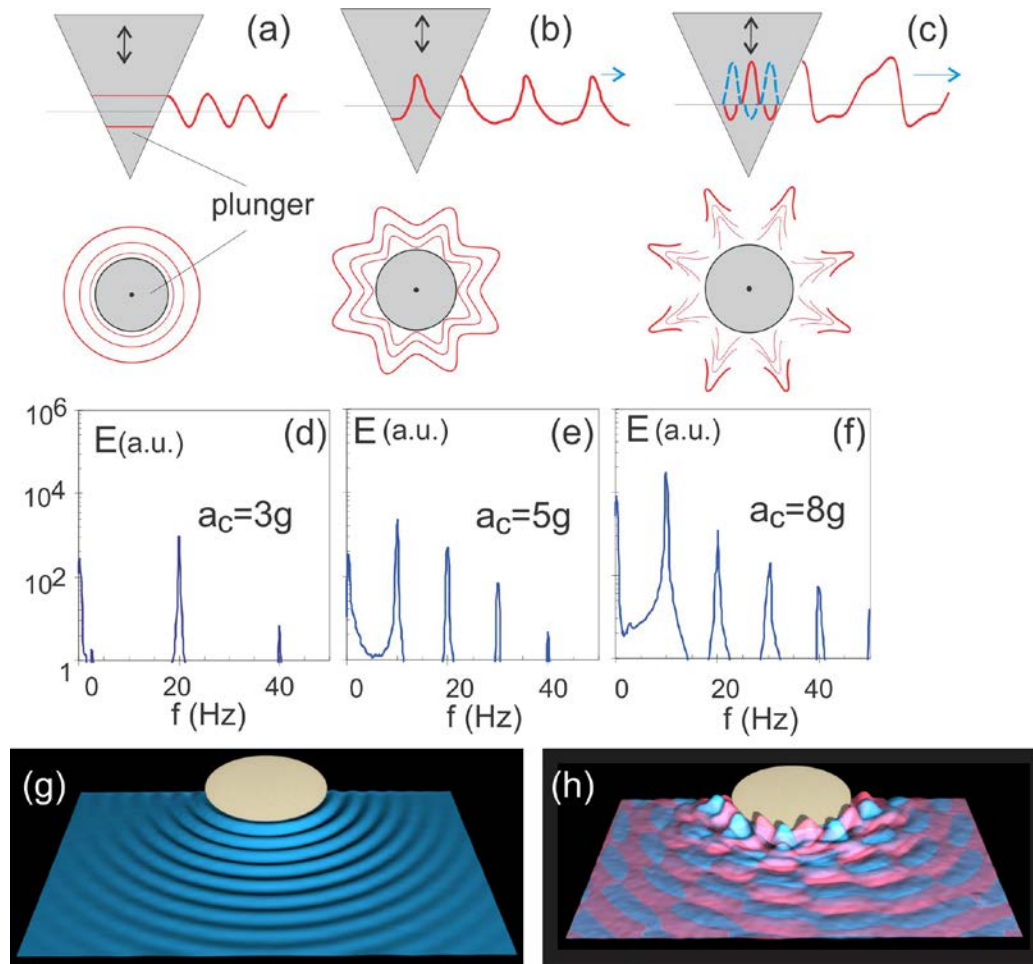
Figure S1 | Schematics of the plunger, waterline and the underwater view of the surface perturbation at (a) $a_c = 3g$, (b) $a_c = 5g$ and (c) $a_c = 8g$. The corresponding frequency spectra of the surface gradient are shown in (d-f). The driving frequency of the plunger is $f_0 = 20$ Hz. The wave fields produced by a conical plunger are visualized using the diffusive light imaging technique at (g) low and (h) higher plunger accelerations. These wave fields correspond to the schematics (a) and (c).

In the main text, the results of Figs. 1 and 2 are obtained using a cylindrical wave maker of a diameter d=25 mm and length L=130 mm. For Figs. 3 and 4 we use a conical plunger having the angle of 60° submerged to the waterline diameter of 50 mm.

Experiments are performed in a rectangular container 1.5×0.5 m^2 filled with water to the level of 80 mm. The wave makers are driven using a 4kN electrodynamic shaker (Bruel&Kjaer). The forcing is sinusoidal and monochromatic. The shaker frequency $f_0 = 20$ Hz corresponds to the wavelength of $\lambda = 12$ mm. The experimental setup is shown in the photograph of Fig. S2.
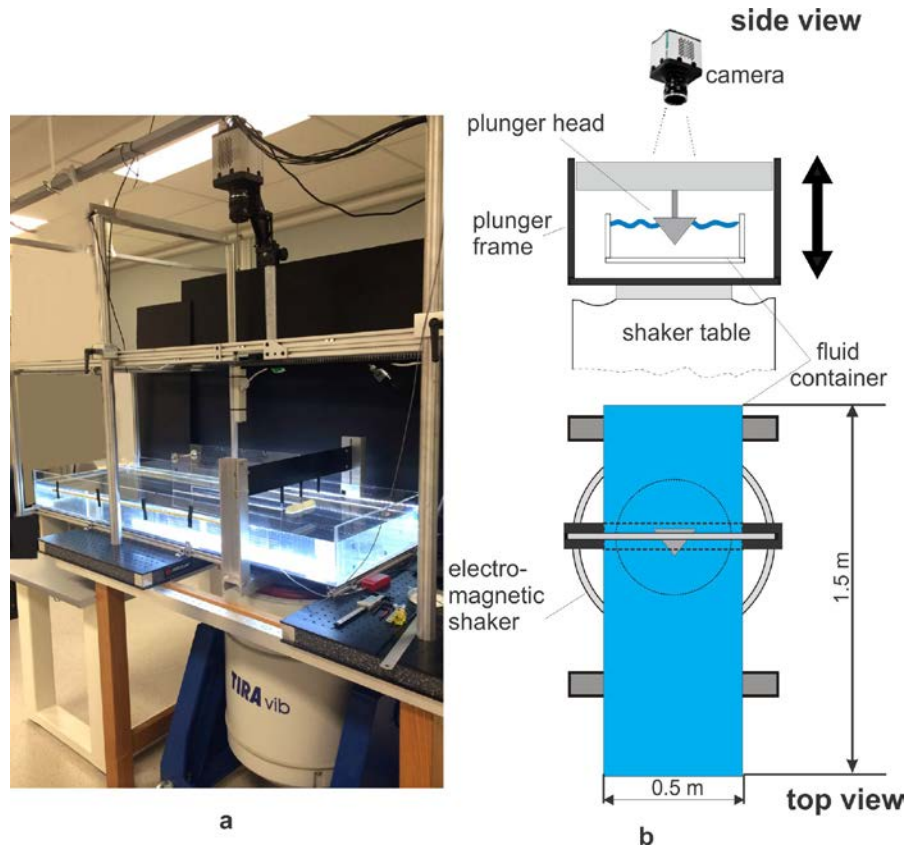
Figure S2 | a Photo and **b** schematics of the experimental setup. A vertically movable plunger is attached to the table of the electromagnetic shaker via the plunger frame. Linear LED arrays on the sides of the transparent water tank illuminate surface particles whose motion is filmed from above using Andor Neo sCMOS camera.

S2 Visualization of particles and waves, particle image velocimetry, and computation of the finite-time Lyapunov exponent.

The flow characteristics are measured using a diffusive light imaging technique, particle image velocimetry and particle tracking velocimetry techniques.

We use the diffusive light imaging to visualize the surface elevation of the wave field [5]. The fluid surface is illuminated by a LED panel placed underneath the transparent bottom of the container. A few percent of milk added to water provides sufficient contrast to obtain a high resolution reconstruction of the wave field. The absorption coefficient is measured before each experiment which allows calibrating the surface elevation with a vertical resolution of 20 μm. Black carbon glass particles are used to visualize the fluid motion on the water surface. During the experiments simultaneous measurements of the surface waves (using diffusive light imaging) and of the floaters horizontal motion are obtained. The particles have diameters within the range 150–300 μm. Alternatively, 50 μm diameter white polyamid particles are used when only the horizontal particle motion needs to be measured.

The use of a surfactant and plasma treatment makes the particle wettability almost neutral. This prevents surface particle clustering and ensures homogeneous spreading on the water surface. Finite particle size effects are negligible under our experimental conditions as discussed in [6].

The diffusive light images and the horizontal particle motion are captured using a high-resolution fast camera (Andor Neo sCMOS). Three-dimensional Lagrangian trajectories are obtained using a combination of two-dimensional particle tracking velocimetry (PTV) technique and a subsequent evaluation of the local elevation along the trajectory. First, horizontal (x-y) coordinates of each point on a trajectory are tracked using a nearest neighbour algorithm [7]. Then, the particle elevation (z coordinate) is estimated as the mean of the wave elevation over a local window (500 μm radius) which is centred on the x-y particle coordinates at a given time. The 3D trajectories of the particle and the wave elevation are visualized using the Houdini 3D animation tools (by Side Effects Software). Figure S3 shows examples of the reconstructed 3D trajectory and the wave elevation field.
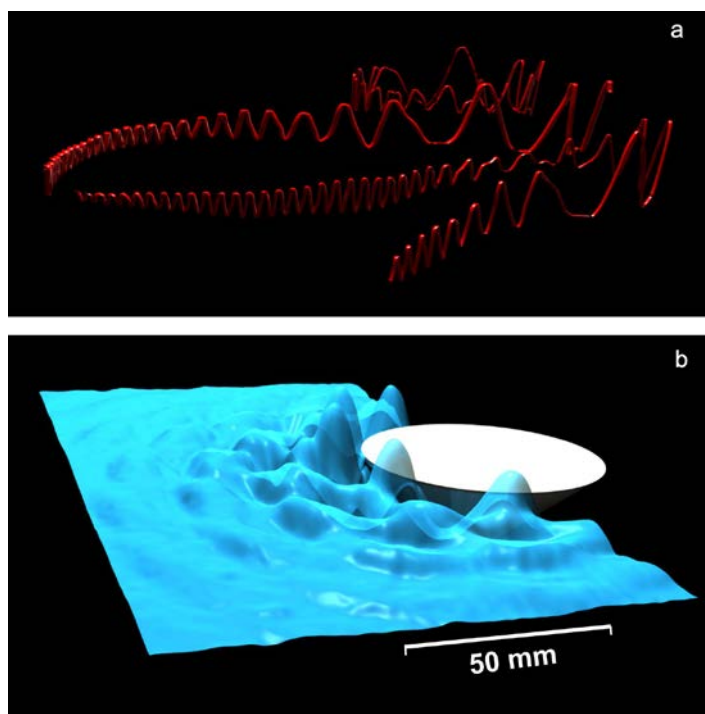

Figure S3 | Examples of (a) reconstructed 3D trajectory recorded for 3s, and (b) reconstructed 3D wave field. A conical plunger (waterline diameter of 48mm) is driven at f_0 = 20 Hz.

The particle image velocimetry (PIV) technique is used to obtain the velocity field of the horizontal motion of the flow. In the experiment described in Fig. 3(c-f), the flow is recorded at 20fps with a spatial resolution of 1850 × 1850 pixels. The velocity fields are computed on a

60×60 grid with 1.2 mm resolution. In the experiments described in Fig. 4(d-f) of the main text, the flow is recorded at 120 fps with a spatial resolution of 512×512 pixels. The PIV velocity fields are computed on a 50×50 spatial grid with 1 mm resolution.

The Lyapunov exponent measures the divergence rate between two adjacent trajectories. A finite-time Lyapunov exponent (FTLE) algorithm has been developed to compute the maximum Lyapunov exponents for the detection of Lagrangian coherent structures [8]. The method is described in Ref. [9]. We use this method to locate the line of maximum divergence in the flow, as shown in Fig. 4(f) in the main text. The PIV velocity fields are interpolated on a refined spatial grid of 600×600 with a time step of Δt=0.002 s. The particle trajectories are obtained by numerical integration using the fourth-order Runge-Kutta method. Each trajectory $\mathbf{x}(t, \mathbf{x}_0)$ starts at a position $\mathbf{x}_0$ at a fixed initial time t_0. By numerical differentiation we compute the largest singular-value field $\lambda_{\max}(t, t_0, \mathbf{x}_0)$ of the deformation-gradient tensor field $[\partial \mathbf{x}(t, t_0, \mathbf{x}_0) / \partial \mathbf{x}_0]^T / [\partial \mathbf{x}(t, t_0, \mathbf{x}_0) / \partial \mathbf{x}_0]$. The FTLE field can be obtained for initial positions $\mathbf{x}_0$ as:

$$\Lambda(\mathbf{x}_0) = [\ln \lambda_{\max}(t, t_0, \mathbf{x}_0)]/(2(t - t_0))$$

S3 Surface flows produced by cylindrical wave makers

As mentioned in the main text, the reversal of the central jet in the nonlinear regime of the wave generation using a cylindrical plunger is a robust effect observed in a broad range of the plunger accelerations with cylinders of various lengths. The stability of the pattern can be optimized by adjusting the excitation frequency, which affects the mode number of the cross wave. The reversal of the jet direction appears to be independent of different driving frequencies. Fig. S4 shows inward flow patterns produced by the cylindrical plunger (white rectangle in the centres of the plots) at two frequencies, in the gravity and in the capillary wave range.
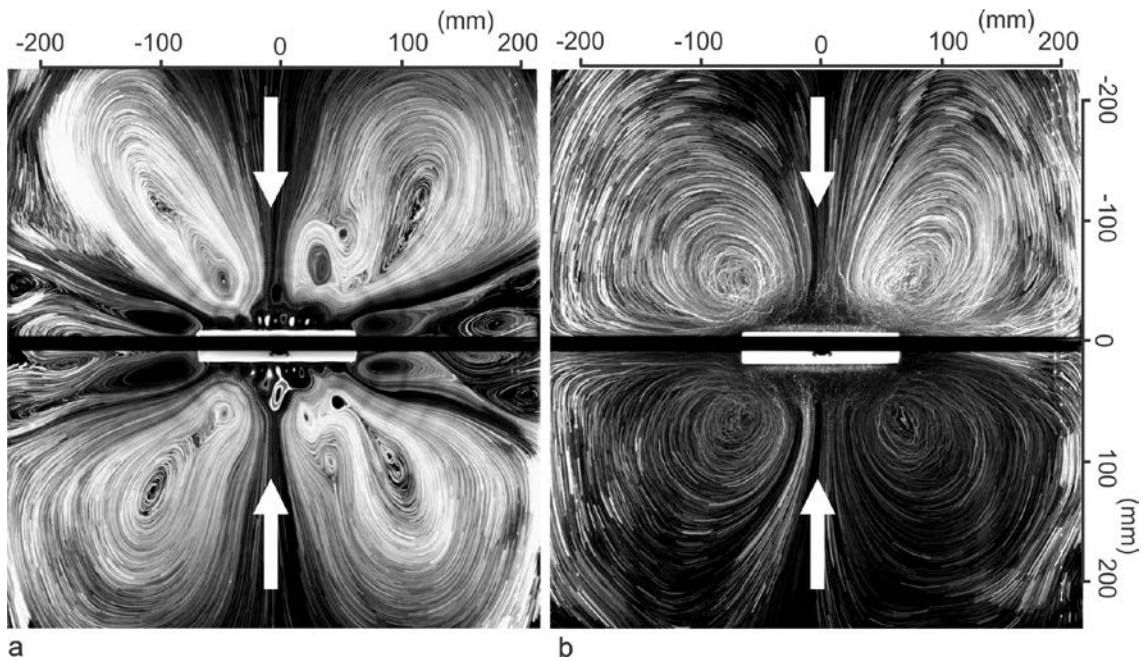
Figure S4 | Inward flow produced by a cylindrical wave maker: (a) nonlinear waves, $f_0 = 20$ Hz, acceleration a_c=2.5g, (b) nonlinear waves, $f_0 = 50$ Hz, acceleration a_c=8.8g.

The velocities of the floaters in both outward and the inward jets have been measured as a function of the distance from the plunger. The velocities of the central jets are shown in Fig. S5 for the regimes corresponding to Figs. 1(a-d) of the main text.
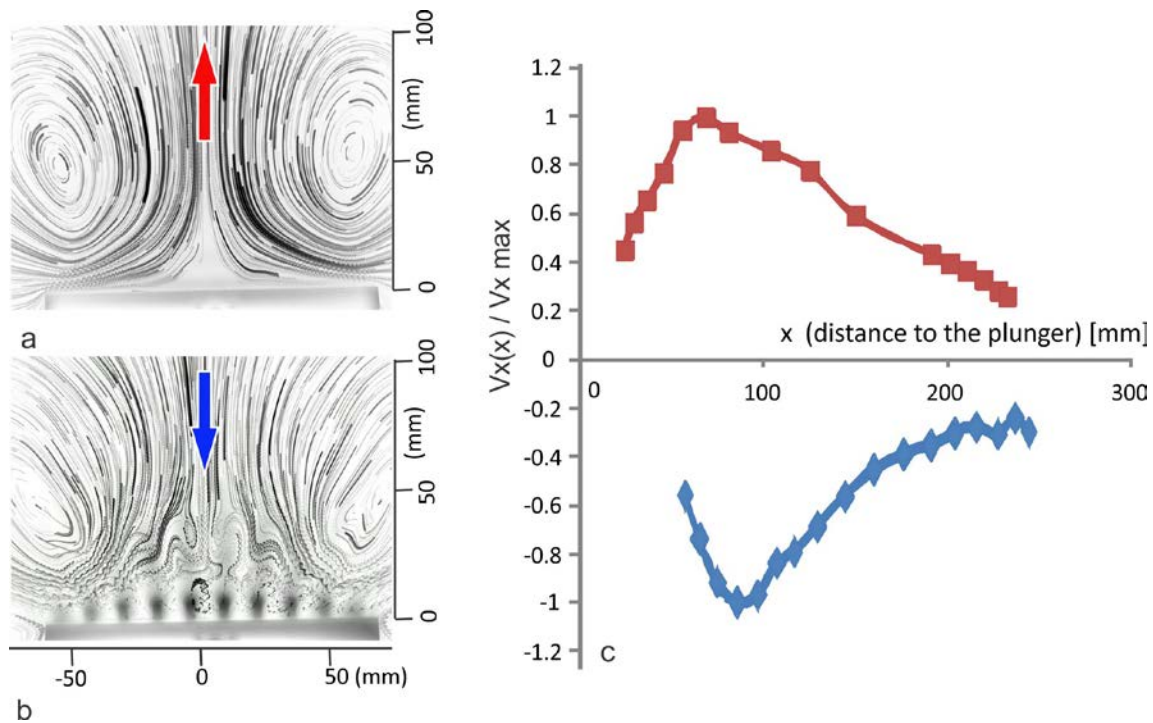
Figure S5 | Structure of the flow produced by the cylindrical plunger (130 mm long) as described in the main text (Figs. 1b,d) for the cases of (a) outward, and (b) inward jets. (c) Measured (normalized) jet velocity versus the distance away from the wave maker. The excitation frequency $f_0 = 20$ Hz.

The motion of floaters on the surface perturbed by capillary-gravity waves propagating away from a wave maker seems inconsistent with the Stokes drift model. This should not be surprising since the original model was developed for planar waves of very small amplitude. However the floaters uniformly move in the direction of the wave propagation in the initial stage of the flow development, before a return flow starts to develop. Surface particle streaks (moving averaged over 5 wave periods) are illustrated in Fig. S6a, where they are filmed shortly after the plunger is activated. During this time most floaters in front of a plunger move in the direction of the wave propagation. However even then their velocities disagree with the Stokes drift expectation, $U_S \sim a^2 k\omega$, where a is the wave amplitude, k and ω are the wave number and frequency. Since the wave amplitude decays away from the plunger, particle velocities should be the highest near the plunger and should decay with the distance. This is not the case, as seen in Fig. S6c. At a later stage, after a stationary flow develops, this discrepancy becomes more pronounced. We conclude that in all wave-driven flows described here, the velocity field is not directly determined by the Stokes drift of the underlying wave field.

The velocity maxima in Figs. S5 and S6 can be considered as separating near-field from far-field flow pattern. In particular, Fig. S6 shows that initially the jet velocity is closer to the wave maker (blue diamonds), while in the steady state (red squares), the velocity profile is broader with the maximum velocity being further away from the plunger. The green triangles in Fig. S6c and the solid line show that the squared wave intensity a^2 strongly decays as a function of the distance from the plunger. This suggests that the flow velocity in not determined by the local wave field, but results from a global flow pattern.
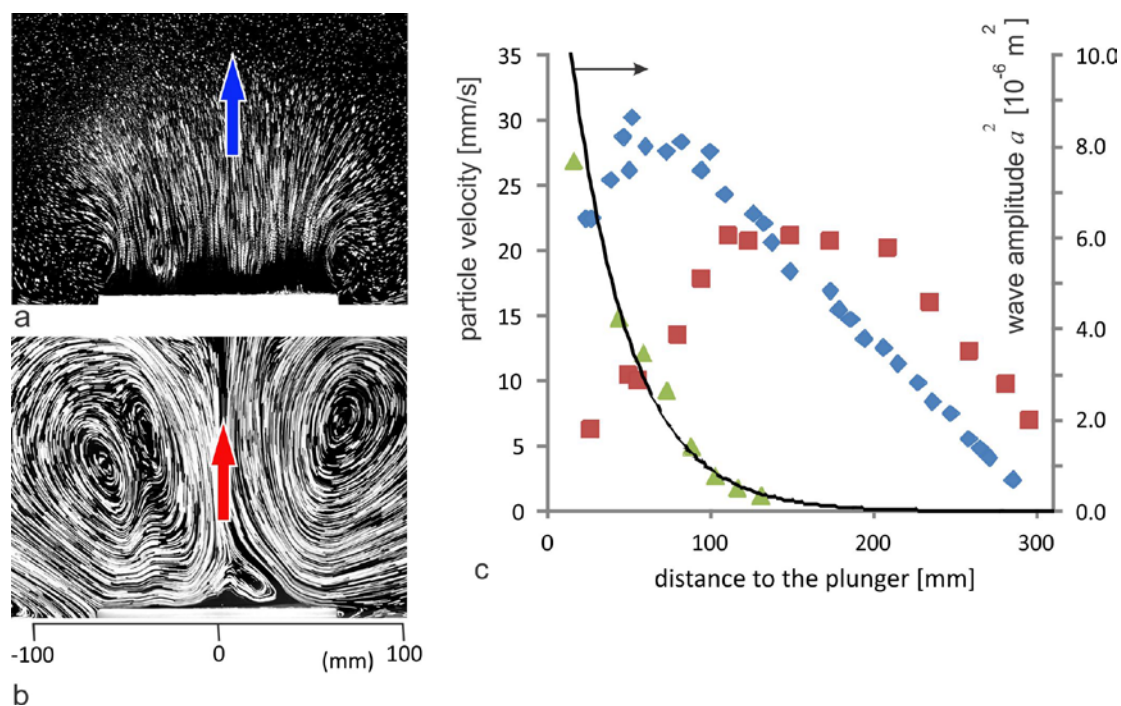

Figure S6 | Surface particle streaks (a) shortly after the plunger is turned on, and (b) in the steady state, after the establishment of a stable quadrupole vortex flow. (c) Central jet velocity as a function of the distance from the wave maker during the start-up phase (diamonds), and in the steady state (squares). Triangles and the solid line show squared wave amplitude a^2 in front of the cylindrical wave maker.

S4   Surface flows produced by various wave makers

As discussed in the main text, stable flow patterns exhibiting inward and outward jets as well as stationary vortices can be generated by appropriately shaping wave makers. Some examples of such flows are shown in Fig. S7.
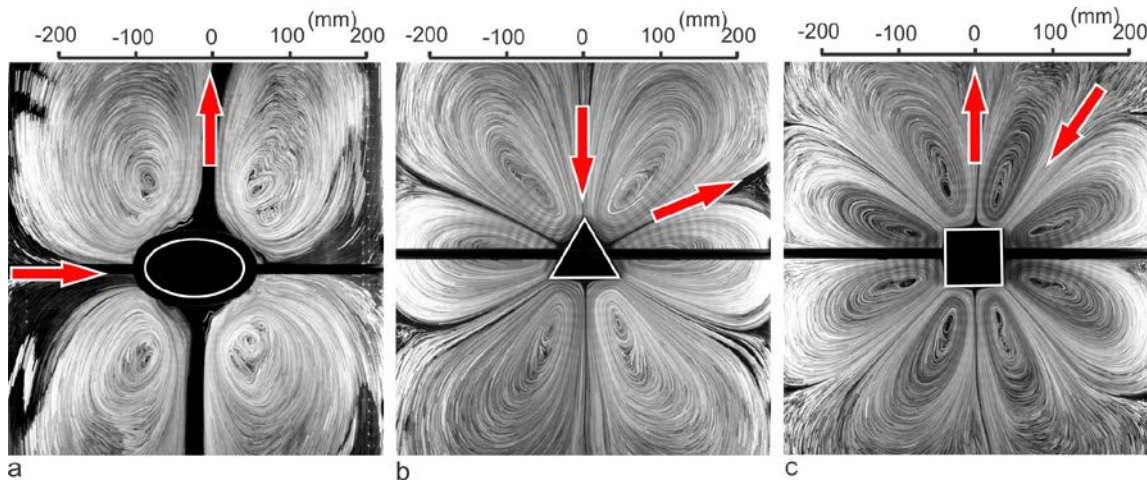
Figure S7 | Surface flow patterns produced by the wave makers of different shapes in the linear regime: (a) elliptical, (c) triangular pyramid, and (d) square pyramid. Waterlines are shown as solid white lines on the plungers. The patterns correspond to the weakly nonlinear waves, below the modulation instability threshold. The excitation frequency in these examples is $f_0 = 60$ Hz.

Similarly to the cylindrical wave maker, pyramidal plungers produce outwards jets normal to the sides of a triangle or a square, while the return flows are directed towards vertices. Above the threshold of modulation instability pyramidal wave makers produce inward central jets and reverse the flow direction. An example of the tractor beam driven by the triangular pyramid is shown in Fig. S8.
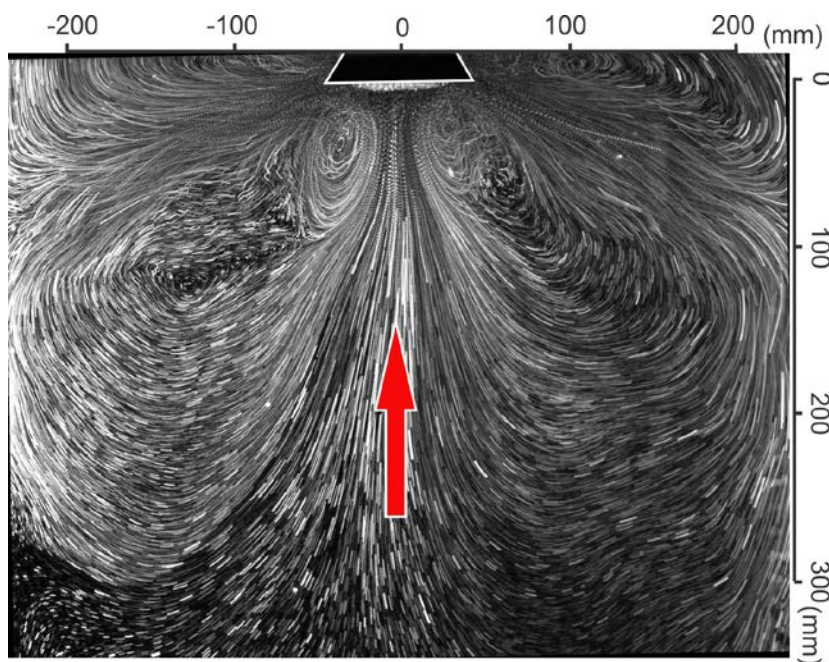

Figure S8 | Visualization of the surface flow produced by a triangular pyramid above the threshold of modulation instability. The wave maker frequency $f = 60$ Hz. The central jet is

directed inward (tractor beam mode). The tractor beam is sufficiently strong to attract small objects, see video "Toy_boat_capture_1fps.mp4". A corresponding flow in the linear regime is shown in Fig. S7b (outward jet).

References:

1. Benjamin, T.B., & Feir, J.E., The disintegration of wave trains on deep water, *J. Fluid Mech.* **27**, 417-430 (1967).

2. Crapper, G.D., An exact solution for progressive capillary waves of arbitrary amplitude, *J. Fluid Mech.* **2**, 532-540 (1957).

3. Xia, H., & Shats, M., Propagating solitons generated by localized perturbations on the surface of deep water, *Phys. Rev. E* **85**, 026313 (2012).

4. Miles, J., and Henderson, D., Parametrically forced surface waves, *Annu. Rev. Fluid Mech.* **22**, 143 (1990).

5. Francois, N., Xia, H., Punzmann, H. & Shats, M. Inverse energy cascade and emergence of large coherent vortices in turbulence driven by Faraday waves. *Phys. Rev. Lett.* **110**, 194501 (2013).

6. Xia H., Francois N., Punzmann H., and Shats M. Lagrangian scale of particle dispersion in turbulence, *Nature Communications*, **4**:2013 doi: 10.1038/ncomms3013 (2013).

7. Crocker, J. C. & Grier, D. G. Methods of digital video microscopy for colloidal studies. *J. Colloid Interface Sci.* **179**, 298–310 (1996).

8. Haller, G., & Yuan, G., Lagrangian coherent structures and mixing in two-dimensional turbulence, *Physica D: Nonlinear Phenomena* **147**, 352-370 (2000).

9. Shadden, S.C., Lejien, F., & Marsden, J.E. Definition and properties of Lagrangian coherent structures from finite-time Lyapunov exponents in two-dimensional aperiodic flows. *Physica D* **212**, 271-304 (2005).